

ADVANCED MATERIALS

Supporting Information

for *Adv. Mater.*, DOI: 10.1002/adma.202105778

Giant Thermal Transport Tuning at a Metal/Ferroelectric Interface

Yipeng Zang, Chen Di, Zhiming Geng, Xuejun Yan,
Dianxiang Ji, Ningchong Zheng, Xingyu Jiang, Hanyu
Fu, Jianjun Wang, Wei Guo, Haoying Sun, Lu Han,
Yunlei Zhou, Zhengbin Gu, Desheng Kong, Hugo
Aramberri, Claudio Cazorla, Jorge Iñiguez, Riccardo
Rurali, Longqing Chen, Jian Zhou, Di Wu, Minghui Lu,*
Yuefeng Nie,* Yanfeng Chen, and Xiaoqing Pan*

Supporting Information

Giant thermal transport tuning at a metal/ferroelectric interface

Yipeng Zang, Chen Di, Zhiming Geng, Xuejun Yan*, Dianxiang Ji, Ningchong Zheng, Xingyu Jiang, Hanyu Fu, Jianjun Wang, Wei Guo, Haoying Sun, Lu Han, Yunlei Zhou, Zhengbin Gu, Desheng Kong, Hugo Aramberri, Claudio Cazorla, Jorge Íñiguez, Riccardo Rurali, Longqing Chen, Jian Zhou, Di Wu, Minghui Lu*, Yuefeng Nie*, Yanfeng Chen & Xiaoqing Pan

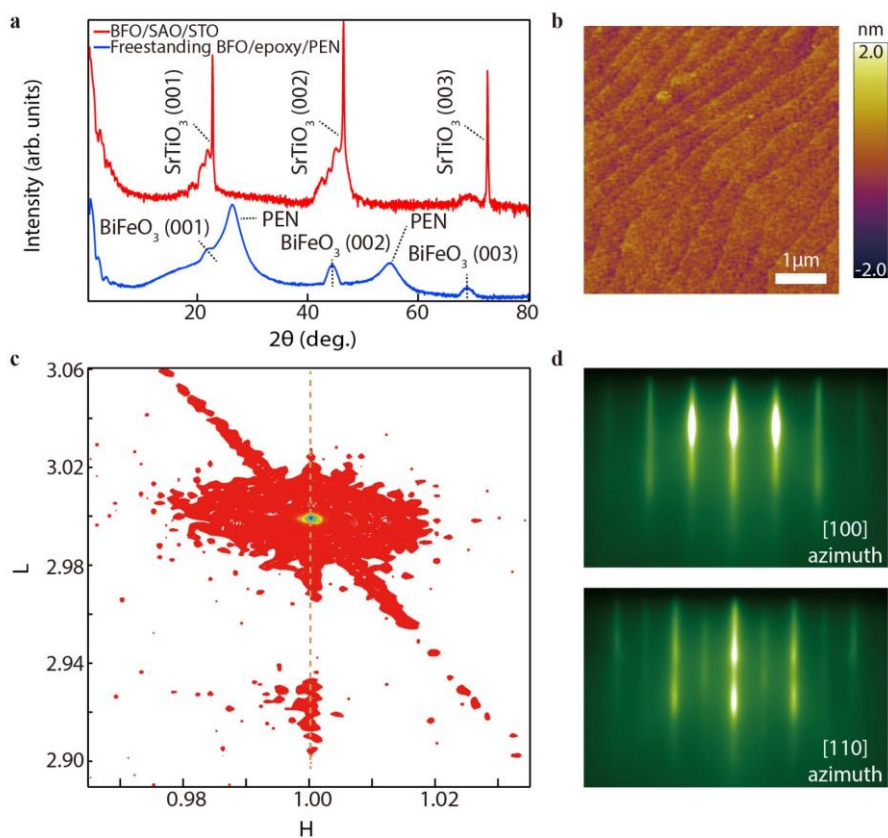


Figure S1 Structure characterizations of as-grown and freestanding BFO films. **a**, 2θ - ω scans of BiFeO₃/Sr₃Al₂O₆/SrTiO₃ (BFO/SAO/STO) and transferred freestanding BFO on PEN. **b**, Topography of freestanding BFO on PEN measured by AFM showing clearly step-and-terrace features. **c**, Reciprocal space mapping of BFO/SAO/STO. **d**, RHEED pattern of the as-grown BFO/SAO/STO with different azimuth orientations.

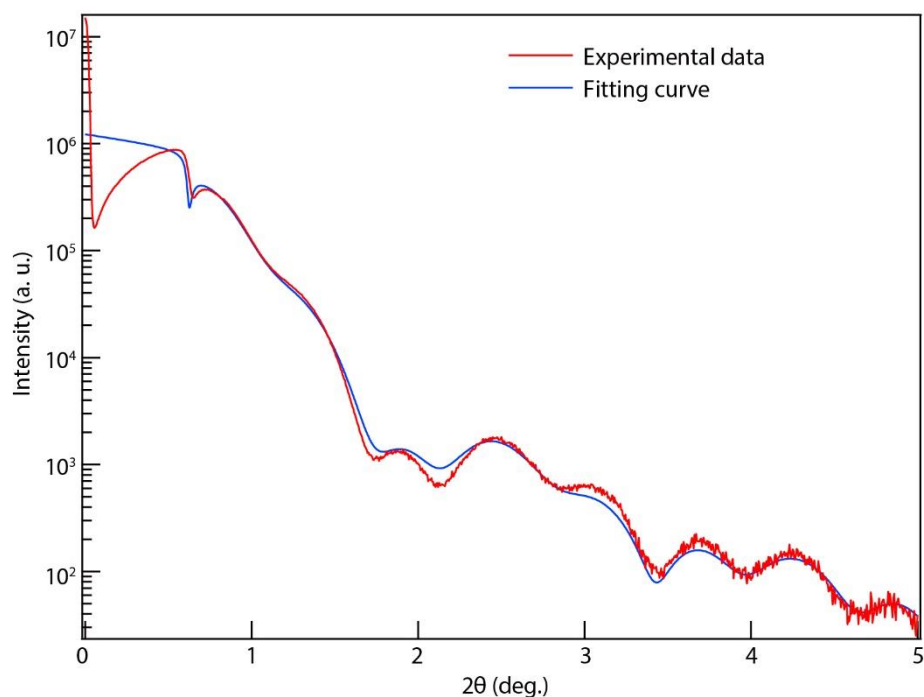


Figure S2 X-ray reflectivity of a BFO/SAO/STO heterostructure. The XRR shows smooth surface of BFO and SAO with fitted thickness of 5.22 nm and 9.31 nm, respectively.

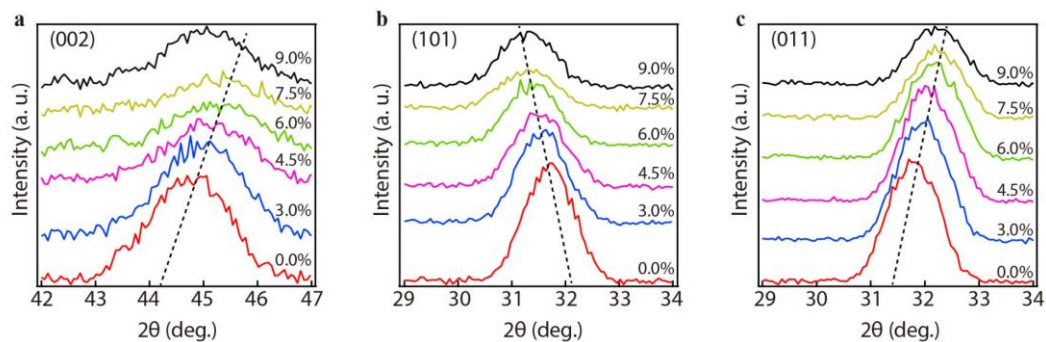


Figure S3 XRD measurements of BFO freestanding films under different uniaxial nominal strain. a-c, The diffraction pattern of (002) plane (a), (101) plane (b) and (011) plane (c) as a function of nominal strain. The evolution of the two theta values implies that a lattice constant increases but the other two lattice constants shrink with uniaxial stretching. The abrupt change at nominal strain of 9.0% is because of the strain relaxation due the formation of microcracks.

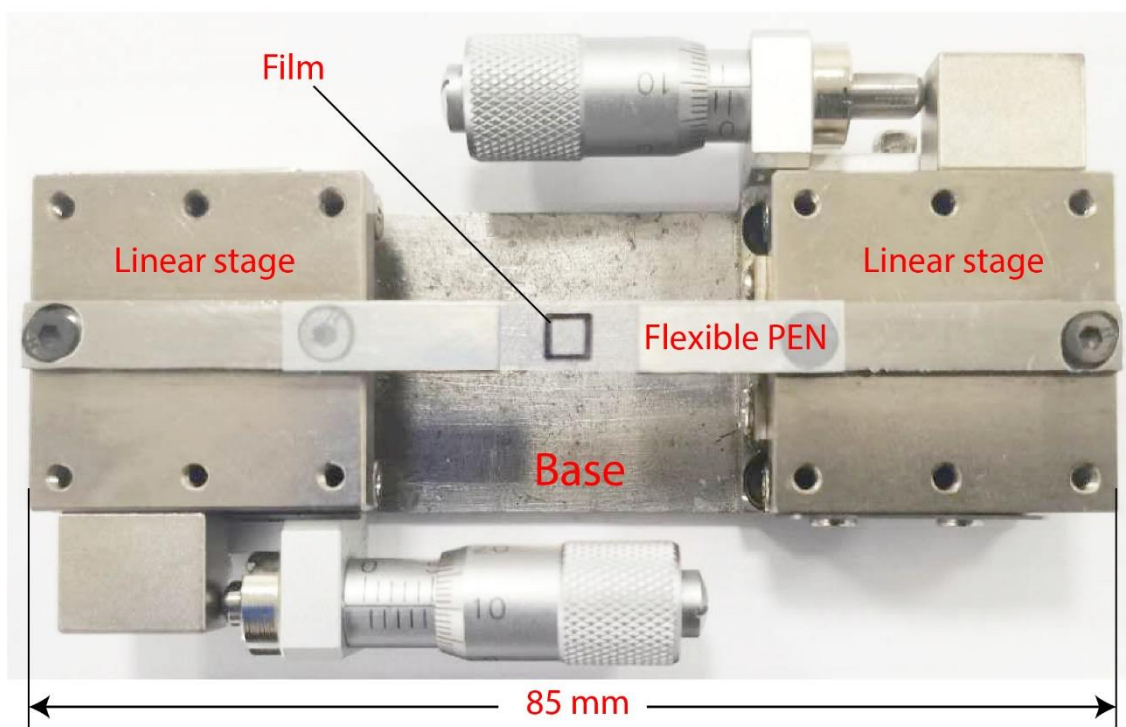


Figure S4 Photo of the stretching device, which includes a base mounted with two linear stages.

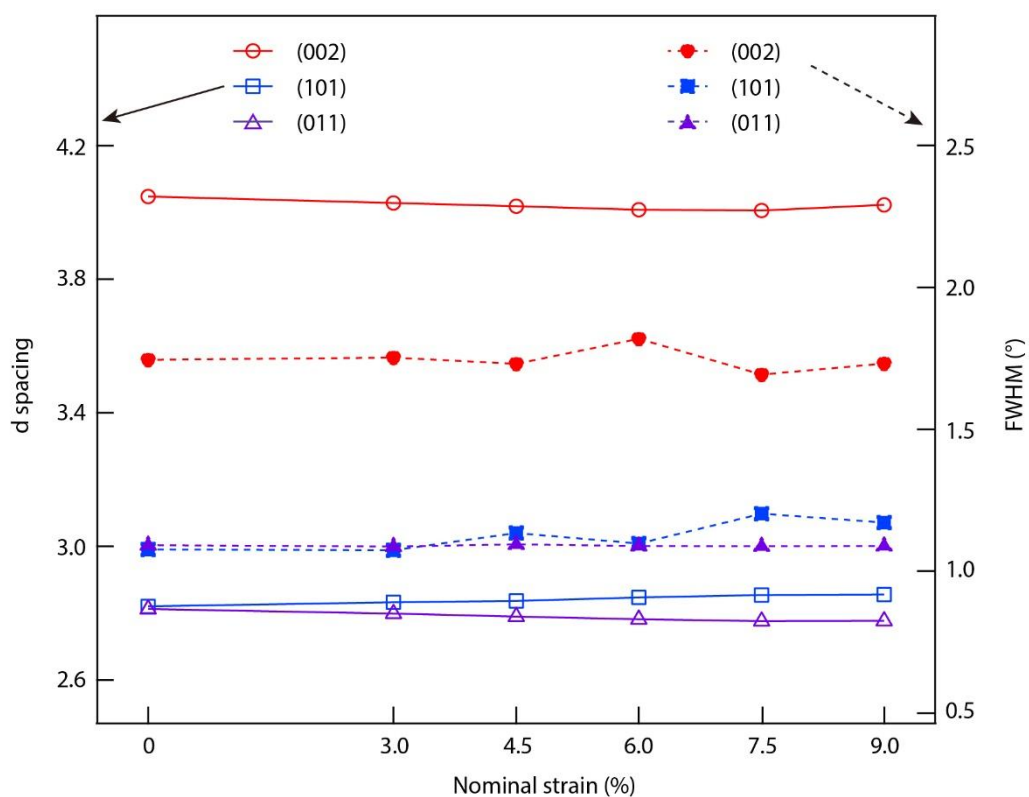


Figure S5 Full Width of Half Maximum (FWHM) of (002) (101) and (011) diffractions and varied d spacing under uniaxial strain. The small variation of FWHM indicates there is no apparent domain migration or lattice slipping take place during strain tuning.

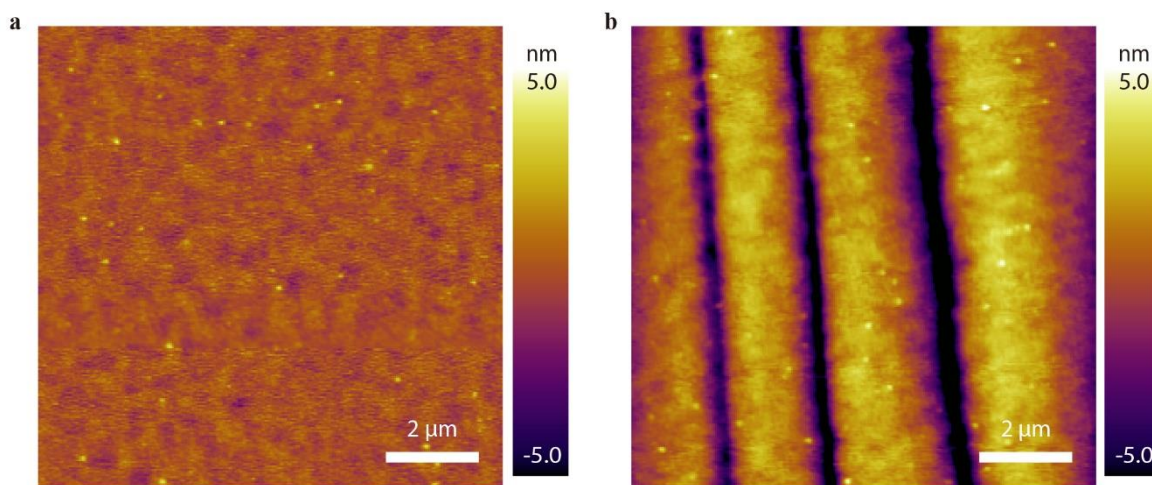


Figure S6 AFM image of BFO films (30 nm) before and after stretching with actual strain of 1.85%. **a-b**, AFM image of BFO films before (a) and after stretching (b), the thicker films are more brittle and form cracks at 1.85% strain.

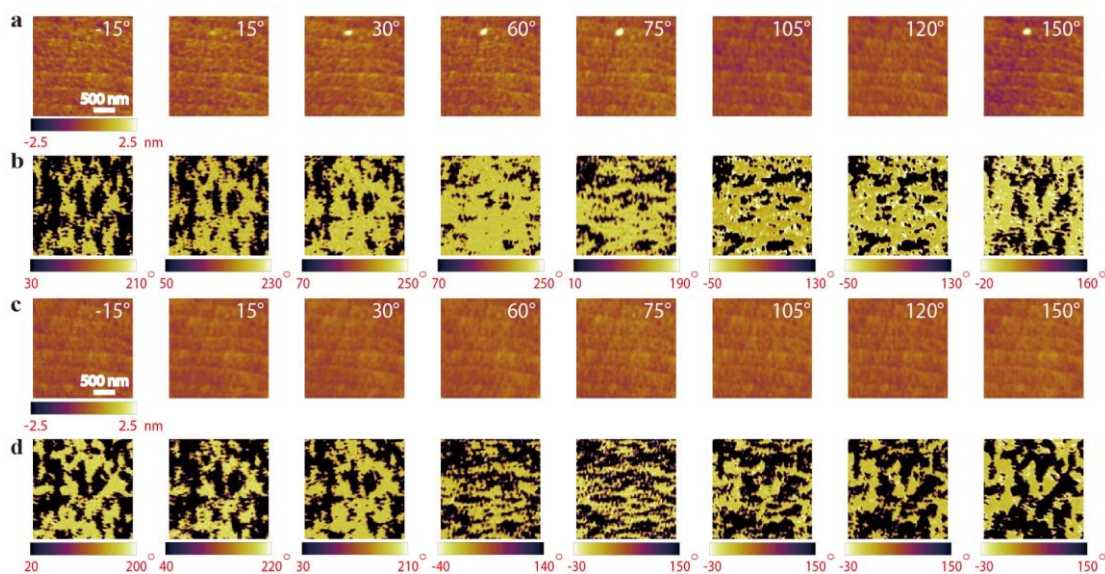


Figure S7 Angle-dependent LPFM measurements on freestanding BFO films. **a-b**, Topography (a) and lateral phase image (b) of BFO films with different rotation angle under initial strain state (0%). **c-d**, Topography (c) and lateral phase image (d) of BFO films with different rotation angle under maximum strain state (3.5%).

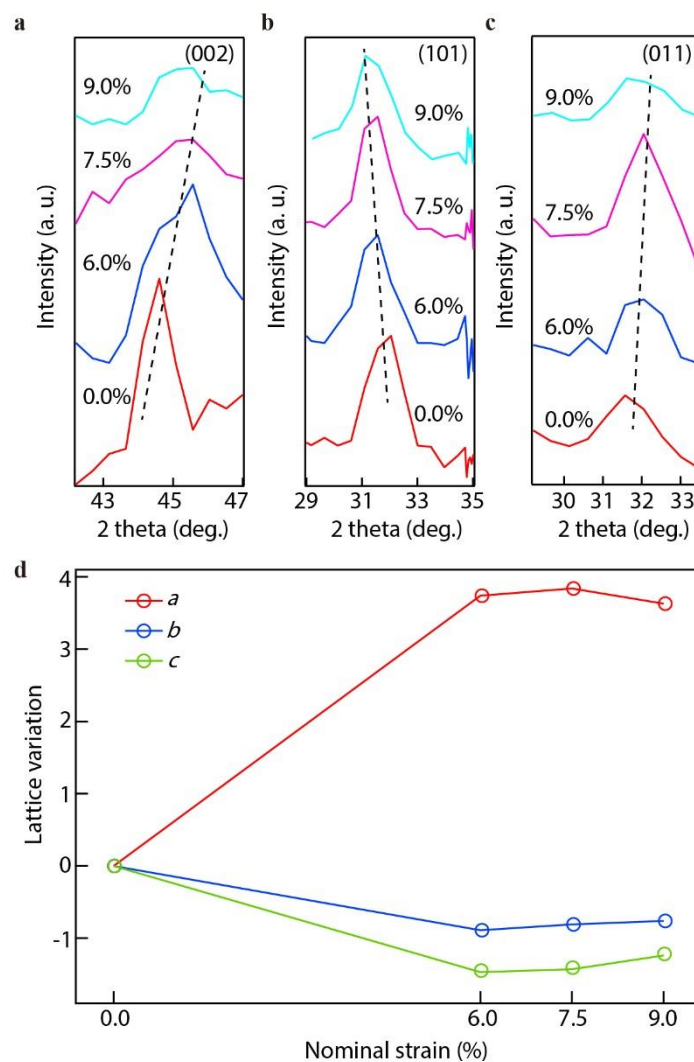


Figure S8 XRD measurements on Al/BFO/Epoxy/PEN structure under different uniaxial nominal strain. a-c, The diffraction pattern of (002) plane (a), (101) plane (b) and (011) plane (c) as a function of nominal strain. **d,** The evolution of the actual lattice parameters under the nominal strain. The maximum strain along the *a* axis is 3.84%, and the Al capping layer does not significantly affect the strain of the BFO film.

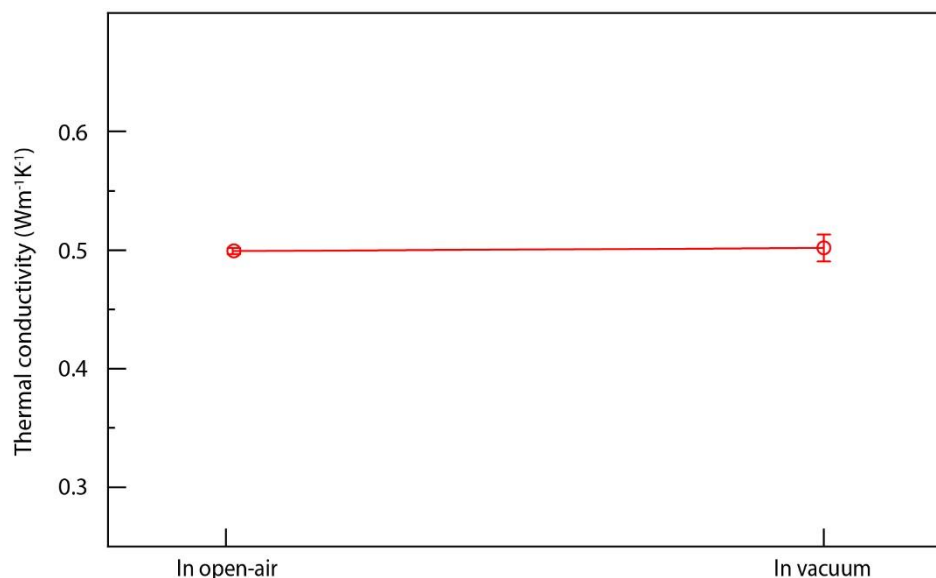


Figure S9 Thermal conductivity of a BFO films (19 nm) measured in open-air and vacuum showing similar results.

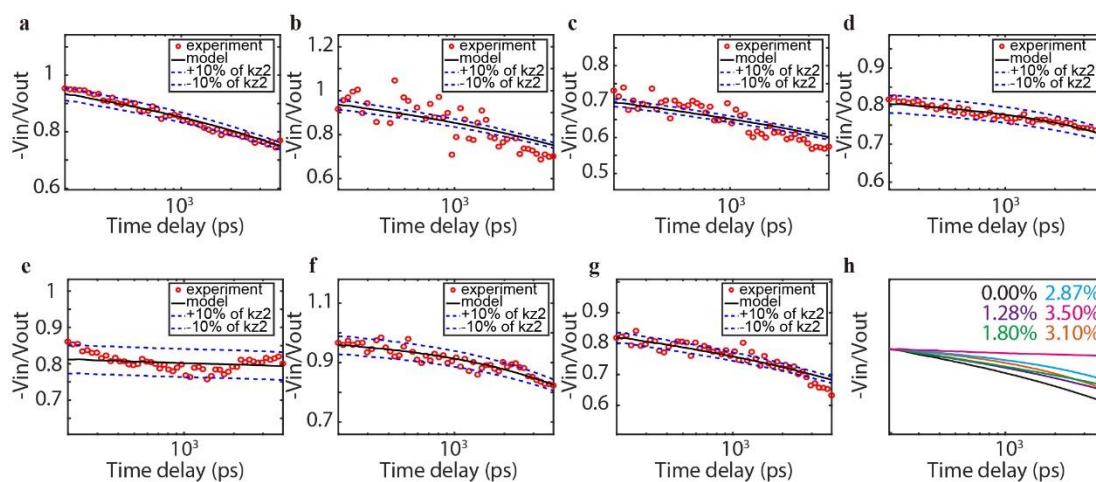


Figure S10 Data fitting of the TDTR measurements for Al/BFO/Epoxy/PEN under different uniaxial strain. The data are taken with uniaxial actual strain of **a**, 0%. **b**, 1.28%. **c**, 1.80%. **d**, 2.87%. **e**, 3.50%. **f**, Released strain-3.10%. **g**, Nominal strain-10.5%. **h**, A plot of fitted curves shows a clear strain-driven change of the thermal conductivity. Note: the curves are shifted along the y axis for a clear comparison.

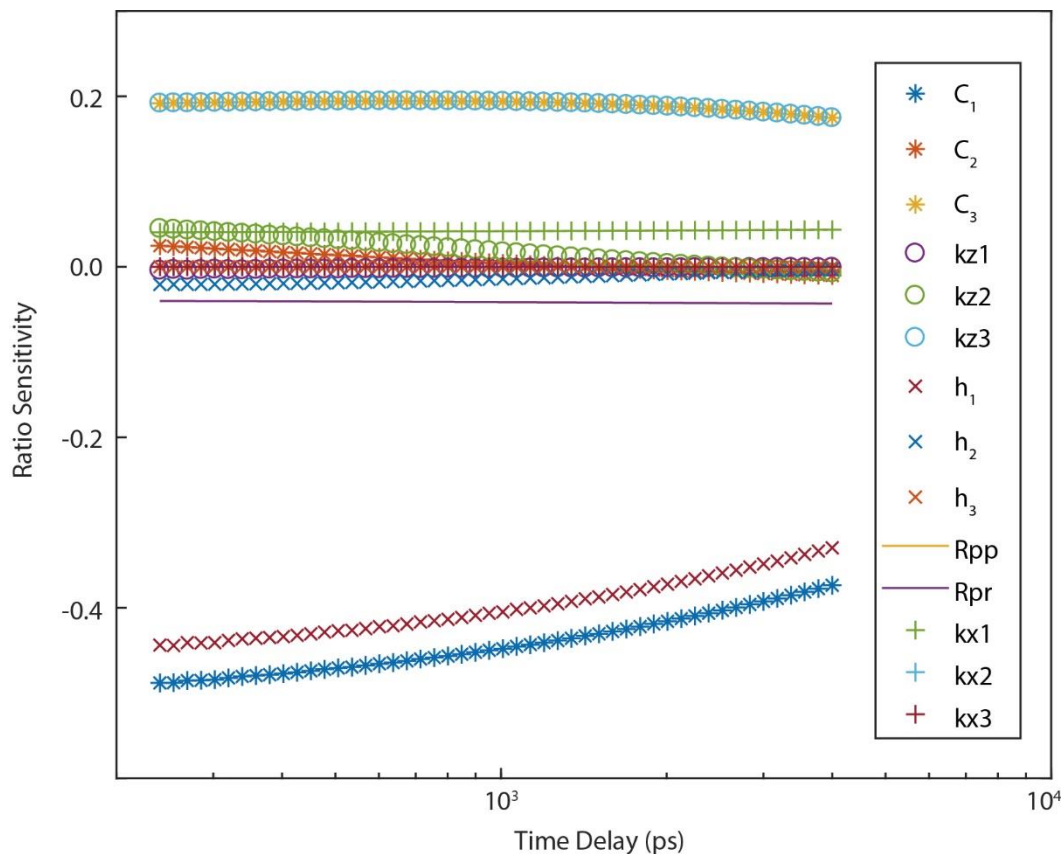


Figure S11 TDTR measurement ratio sensitivities of volumetric heat capacity, thermal conductivity and thickness of each layer against delay time in Al/BFO/Epoxy/PEN heterostructure. Ratio sensitivity (S_α) denotes how sensitive the signals are to the physical parameter α (such as thermal conductivity, volumetric heat capacity and thickness of each layer); a higher sensitivity of the sample thermal conductivity should be preferred. Herein, the subscript 1 denotes Al, 2 denotes BFO and 3 denotes epoxy. It can be seen that among all the fitting parameters (that is to say, the cross-plane thermal conductivities of BFO K_{z2} and epoxy K_{z3}), sensitivity of K_{z2} are relatively high. This directly proves that the method is sensitive enough to measure the thermal properties of BFO films.

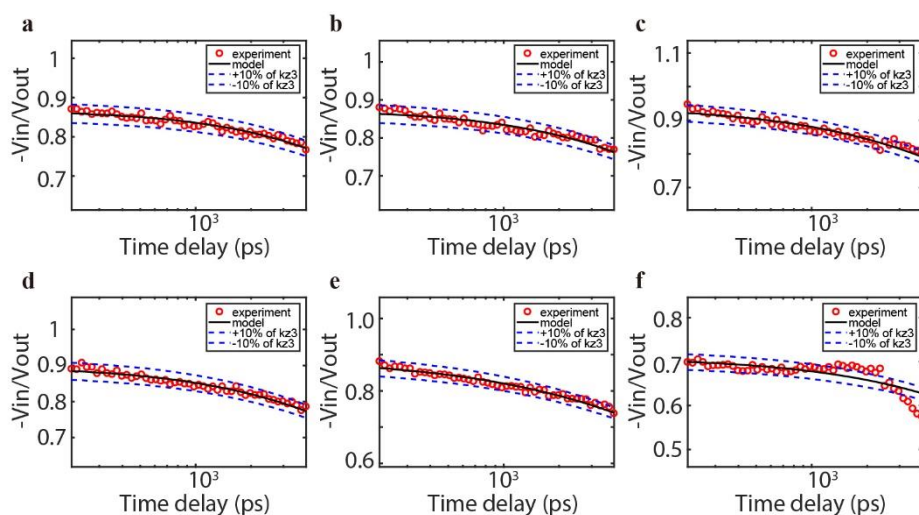


Figure S12 Data fitting of the TDTR measurement for Al/Epoxy/PEN under different uniaxial strain. The data are taken with uniaxial strain of **a**, 0%. **b**, 1.0%. **c**, 2.0%. **d**, 3.0%. **e**, 4.5%. **f**, 6.0%.

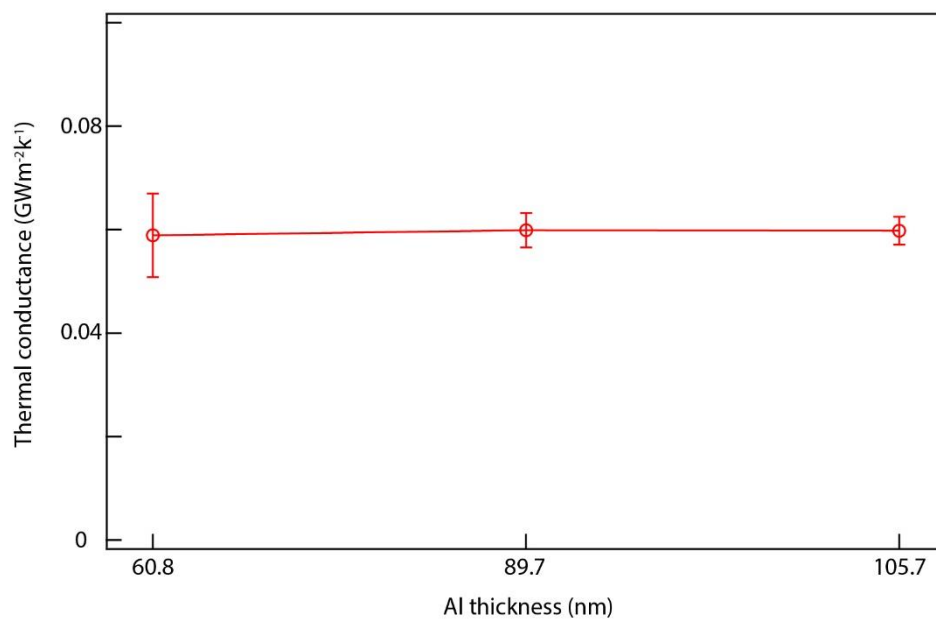


Figure S13 Thermal conductance of Al/BFO interface with varying Al thicknesses. The thickness of Al layer does not significantly affect the interfacial thermal conductance.

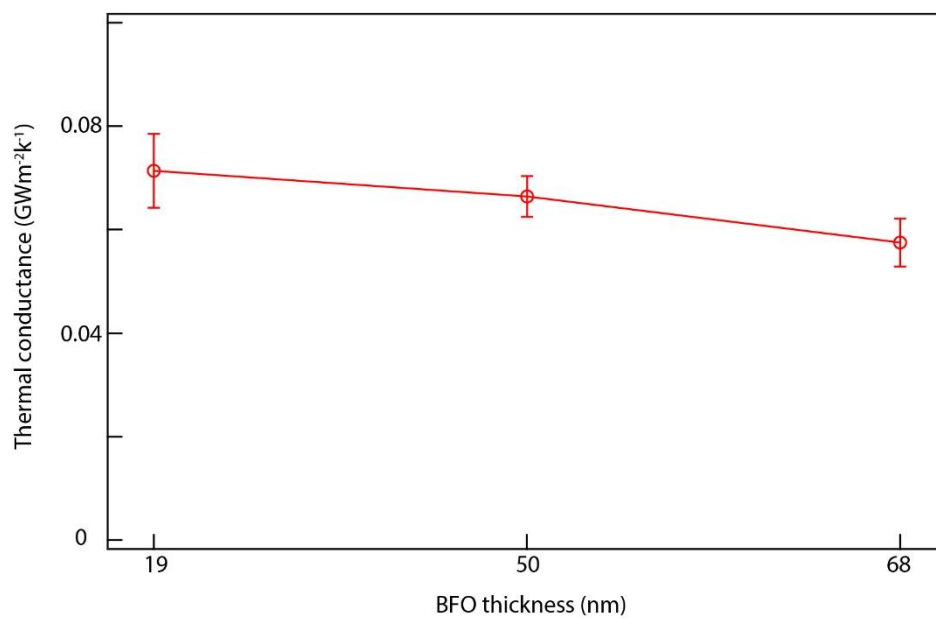


Figure S14 Thermal conductance of Al/BFO interface with varying BFO thicknesses. The thickness of BFO layer only slightly affect the interfacial thermal conductance.

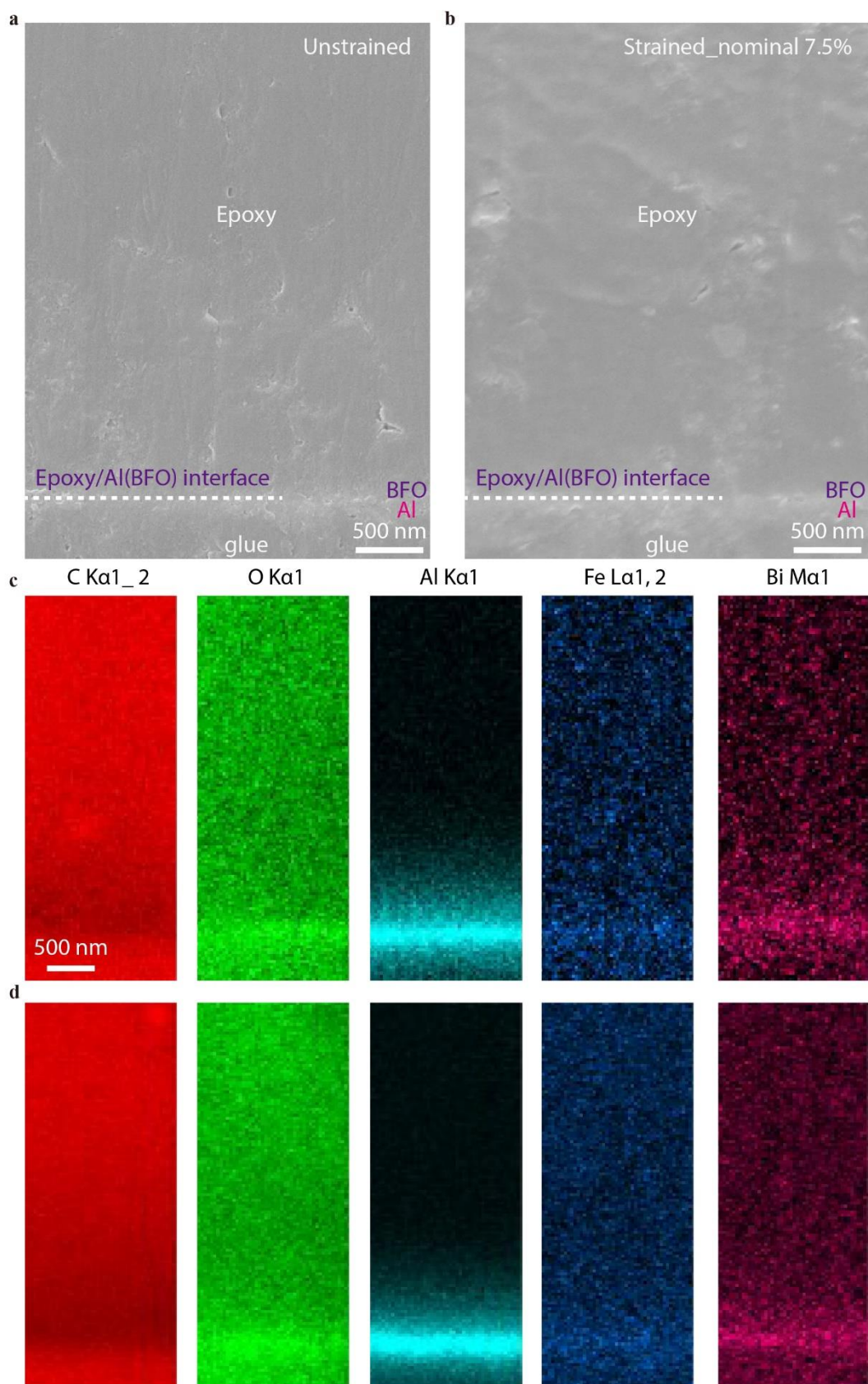


Figure S15 Cross-sectional SEM and EDS images of Al/BFO/Epoxy before and after stretching. **a-b**, Cross-sectional SEM images before stretching (a) and after stretching with a nominal strain of 7.5% (b). **c-d**, Cross-sectional EDS images before stretching (c) and after stretching with a nominal strain of 7.5% (d).

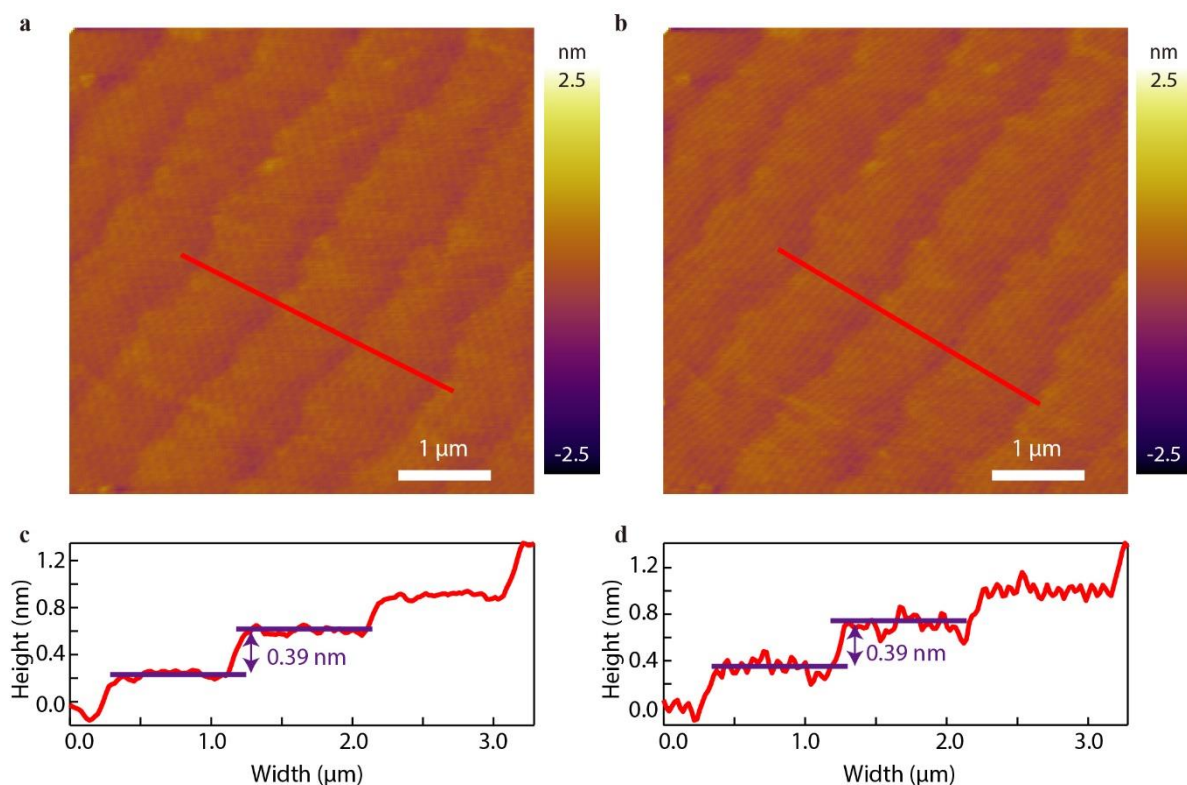


Figure S16 Surface topology state of epoxy layer before and after stretched with nominal strain of 7.5%. a-d, AFM image and height profile of epoxy before (a, c) and after (b, d) stretching show an atomically smooth step-and-terrace surface.

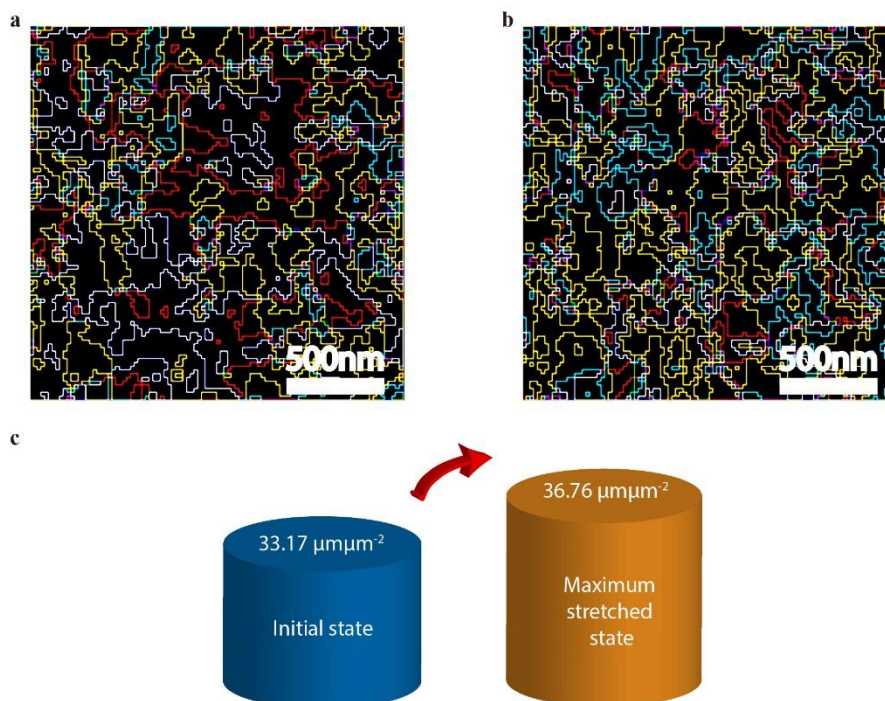


Figure S17 Variation of the in-plane domain wall density in freestanding BFO films before and after stretching. a-c, Domain wall density is changed from $33.17 \mu\text{m}\mu\text{m}^{-2}$ under initial strain state_0% (a, c) to $36.76 \mu\text{m}\mu\text{m}^{-2}$ under maximum strain state_3.5% (b, c). Domain wall density is defined as the domain wall length per unit area and mentioned in an earlier paper^[1].

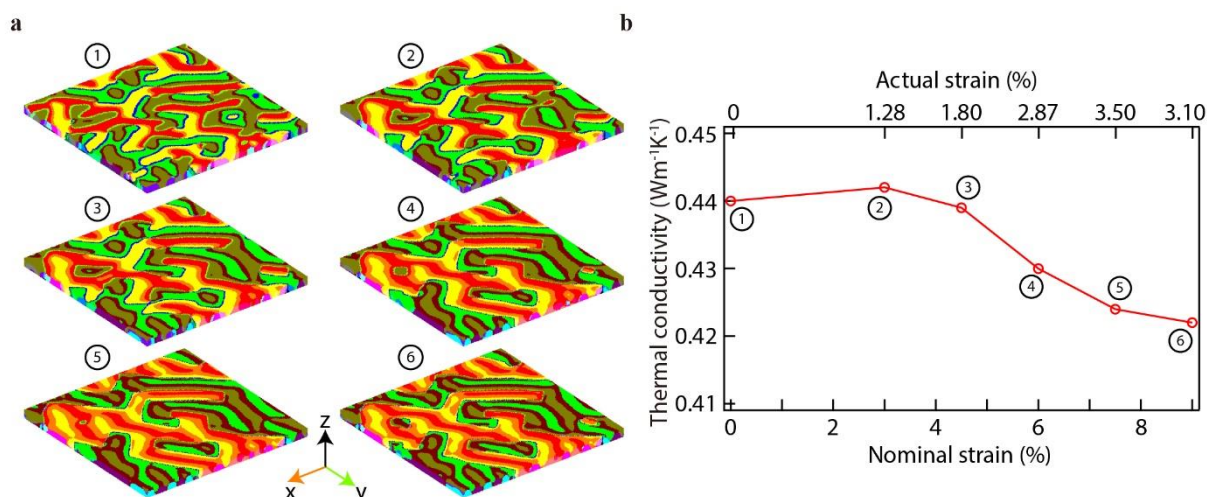


Figure S18 Phase field simulations of the domain pattern and thermal conductivity of BFO. **a**, Domain structure evolution as a function of strain showing only small changes of the domain wall density. **b**, Thermal conductivity of BFO films under different strain state showing only minor changes ($\sim 4\%$) by applying uniaxial strain. Note that the thermal conductivity only considers the contribution from the domain wall density as described in the literature^[2].

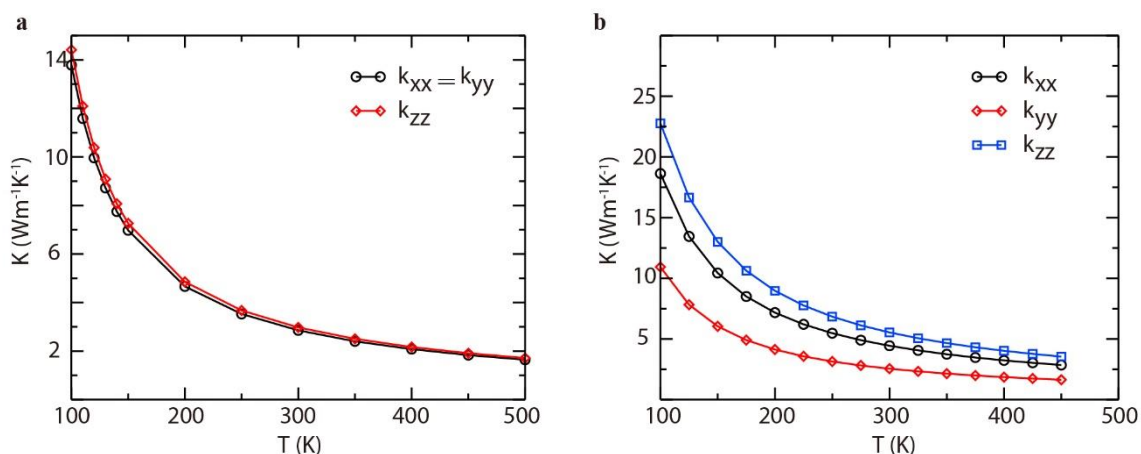


Figure S19 First-principles calculations of the thermal conductivity of monodomain bulk BFO. **a**, Calculated thermal conductivity of unstrained R3c-BFO showing negligible anisotropy. **b**, Diagonal terms of the thermal conductivity tensor under uniaxial strain applied along the y-axis of Cc-BFO. Taking into account the contribution of off-diagonal terms we obtain a thermal conductivity along the direction probed in the experiments of $2.93 \text{ Wm}^{-1}\text{K}^{-1}$, to be compared with $2.97 \text{ Wm}^{-1}\text{K}^{-1}$ in the unstrained R3c cell, which is in sharp contrast to the observation of the decrease of thermal conductivity in our experiments. Note that these results refer to bulk BFO and do not consider any boundary scattering term.

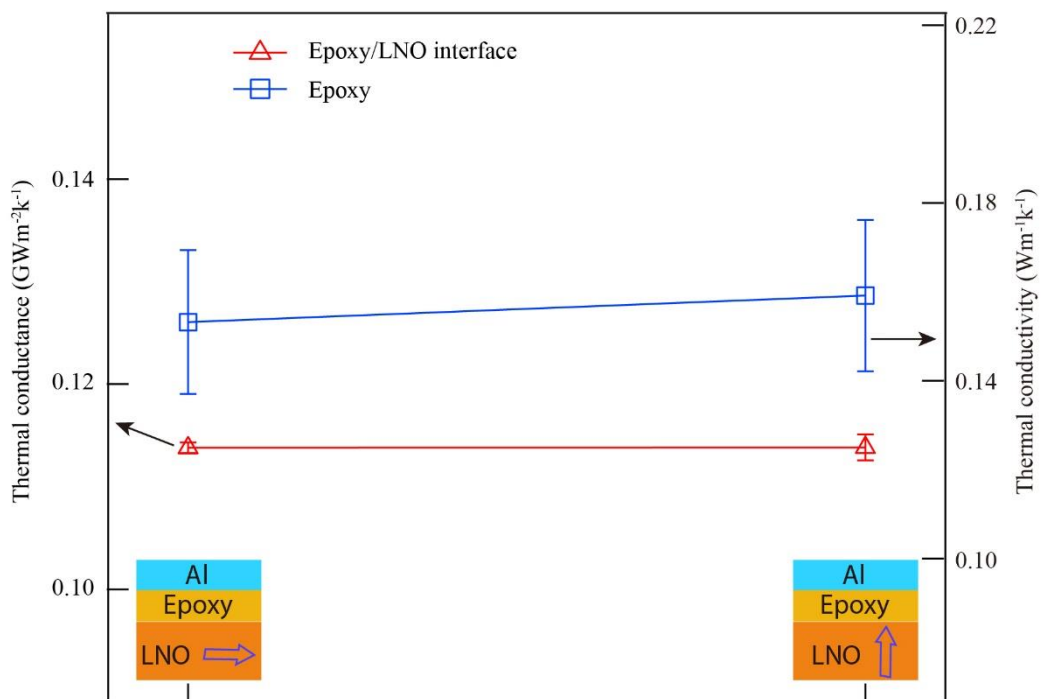


Figure S20 Thermal conductance/conductivity of Epoxy/LNO interface (red line) and Epoxy (blue line) with varied LNO polarization direction. The polarization direction of the LNO has no obvious effect on the Epoxy/LNO interfacial thermal conductance.

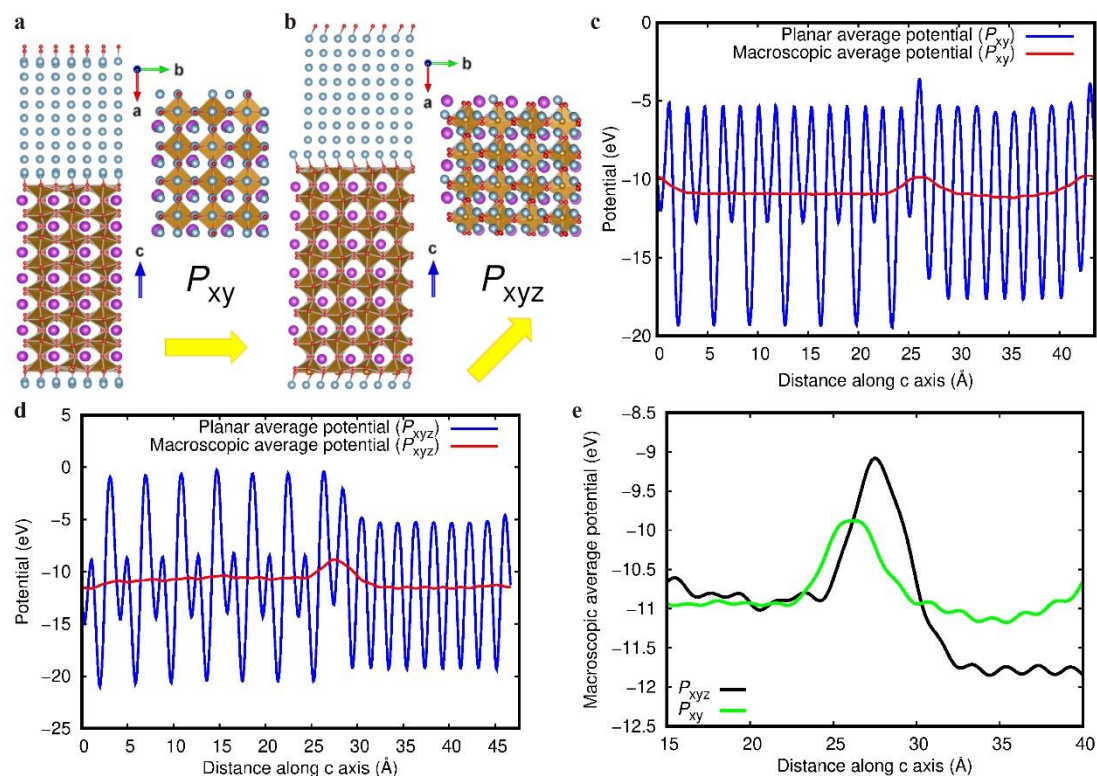


Figure S21 First-principles estimate of the electric dipole created at the Al/BFO system as a function of the BFO ferroelectric polarization orientation. **a**, Atomistic representation of the simulated Al/BFO system in which the BFO electric polarization is oriented parallel to the metal/ferroelectric interface. **b**, Equivalent to **a** but the BFO polarization now is oriented along the pseudocubic [111] direction. Al, Bi, Fe, and O ions are represented with blue, purple, brown and red spheres. The yellow arrows indicate the orientation of the BFO electric polarization relative to the Al/BFO interface. **c**, Planar and macroscopic average potentials estimated along the direction perpendicular to the Al/BFO interface for the system represented in **a**. **d**, Planar and macroscopic average potentials estimated along the direction perpendicular to the Al/BFO interface for the system represented in **b**. **e**, Magnification of the macroscopic average potential estimated at the Al/BFO interface for the two systems represented in **a** and **b**. The larger macroscopic average peak calculated for the interface system in which the BFO polarization is not parallel to the metal/ferroelectric interface, is identified with a larger accumulation of bound charges in the BFO side and of free screening charges in the metallic Al side.

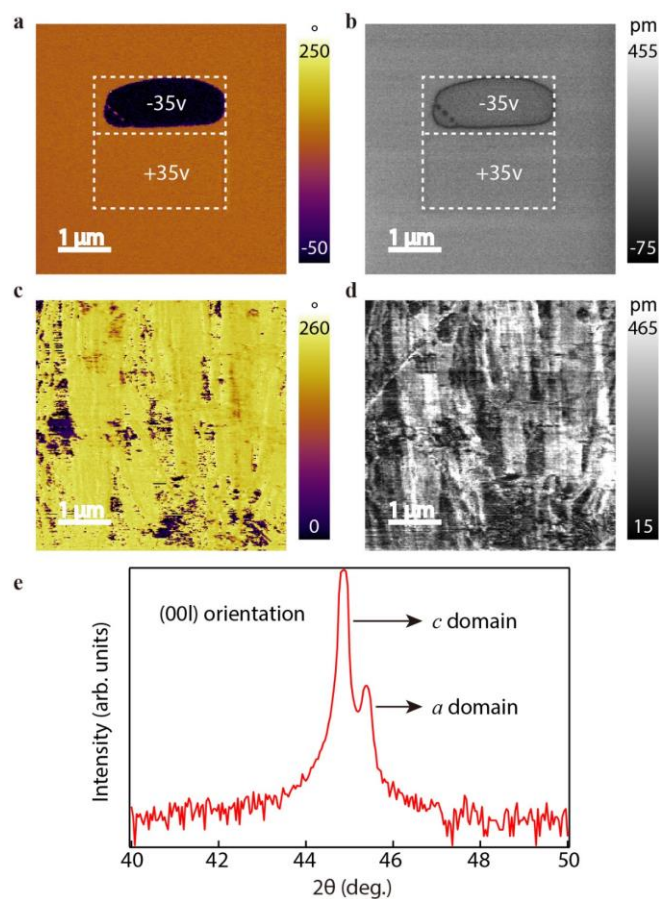


Figure S22 Ferroelectric domain structure in BaTiO₃ single crystal. **a**, PFM phase image of the out-of-plane polarization showing nearly single phase. Inset shows the domain writing to determine the original polarization direction. **b**, PFM amplitude image of the out-of-plane polarization. **c**, phase image of the in-plane polarization. **d**, PFM amplitude image of the in-plane polarization. **e**, 2θ-ω scans along the (00L) direction showing the coexistence of *a*-domain and *c*-domain.

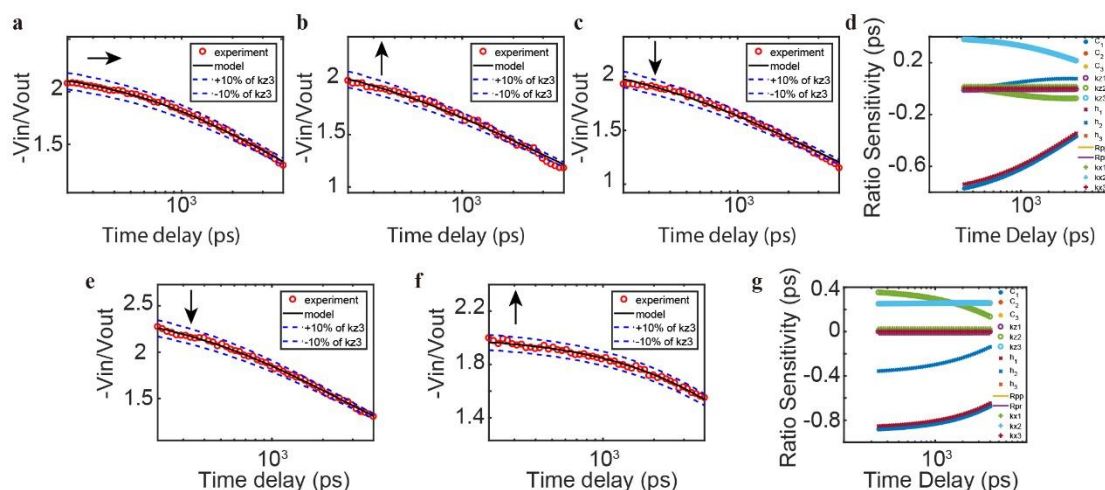


Figure S23 Data fitting of the TDTR measurement for Al/BTO and Al/LNO with different polarization directions, and ratio sensitivity of the measurements. **a**, LNO-in plane polarization, **b**, LNO-upward polarization, **c**, LNO-downward polarization, **e**, BTO-downward polarization, **f**, BTO-upward polarization. **d-g**, Ratio sensitivity for Al/LNO (d) and Al/BTO (g), K_{z1} represents Al, K_{z2} represents Al/ferroelectric interface and K_{z3} represents LNO or BTO.

Table S1 Fitting parameters for Al, BFO, BTO, Epoxy and LNO.

Sample	Volumetric Specific Heat [$Jcm^{-3}K^{-1}$]	Reference
Al	2.42	https://cahill.matse.illinois.edu/software-and-data
BFO	2.88	[3]
BTO	2.68	[4]
Epoxy	2.07	[5]
LNO	2.80	[6]

References

- [1] P. E. Hopkins, C. Adamo, L. H. Ye, B. D. Huey, S. R. Lee, D. G. Schlom, J. F. Ihlefeld, *Appl. Phys. Lett.* **2013**, 102, 121903.
- [2] E. Langenberg, D. Saha, M. E. Holtz, J. J. Wang, D. Bugallo, E. Ferreira-Vila, H. Paik, I. Hanke, S. Ganschow, D. A. Muller, L. Q. Chen, G. Catalan, N. Domingo, J. Malen, D. G. Schlom, F. Rivadulla, *Nano Lett.* **2019**, 19, 7901.
- [3] Y. Wang, J. E. Saal, P. P. Wu, J. J. Wang, S. L. Shang, Z. K. Liu, L. Q. Chen, *Acta Mater.* **2011**, 59, 4229.
- [4] B. A. Strukov, S. T. Davitadze, S. N. Kravchun, S. A. Taraskin, M. Goltzman, V. V. Lemanov, S. G. Shulman, *J Phys Condens Matter* **2003**, 15, 4331.
- [5] F. Lin, G. S. Bhatia, J. D. Ford, *J. Appl. Polym. Sci.* **1993**, 49, 1901.
- [6] S. H. Yao, J. Y. Wang, H. Liu, X. B. Hu, H. J. Zhang, X. F. Cheng, Z. C. Ling, *J. Alloys Compd.* **2008**, 455, 501.